RSC Advances

PAPER

View Article Online
View Journal | View Issue

Cite this: *RSC Adv.*, 2023, **13**, 17428

# Spherical $Fe_7S_8$@rGO nanoflowers as electrodes with high electrocatalytic performance in dye-sensitized solar cells†

Xiaoyu Wang,[a] Wen Wang,[a] Jixin Yao,[c] Qingxiao Zhang,[a] Xin Gao,[a] Changcheng Lin,[a] Qun Yang,[b] Xueqin Zuo,[b] Shaowei Jin *[ab] and Guang Li *[a]

Received 13th April 2023
Accepted 1st June 2023

DOI: 10.1039/d3ra02457a

rsc.li/rsc-advances

Dye-sensitized solar cells (DSSCs) can directly convert solar energy into electricity, and have aroused great research interest from researchers. Here, the spherical $Fe_7S_8$@rGO nanocomposites were expediently fabricated by facile methods, and applied in DSSCs as counter electrodes (CEs). The morphological features show the porous structure of $Fe_7S_8$@rGO, and it is beneficial to enhance the permeability of ions. Reduced graphene oxide (rGO) has a large specific surface area and good electrical conductivity, shortening the electron transfer path. The presence of rGO promotes the catalytic reduction of $I_3^-$ ions to $I^-$ ions and reduces the charge transfer resistance ($R_{ct}$). The experimental findings show that the power conversion efficiency (PCE) of $Fe_7S_8$@rGO as CEs for DSSCs can reach 8.40% (20 wt% for rGO), significantly higher than $Fe_7S_8$ (7.60%) and Pt (7.69%). Therefore, $Fe_7S_8$@rGO nanocomposite is expected to be an efficient and cost-effective CE material for DSSCs.

## 1. Introduction

The overconsumption of minerals results in environmental degradation and energy crisis, thus more and more scientists are working on clean, renewable energy sources in order to overcome these problems.[1,2] Solar energy is a natural and renewable energy that can alleviate the need for clean energy. Dye-sensitized solar cells (DSSCs) convert radiant energy into electrical energy by simulating photosynthesis in plants.[3,4] This energy conversion device has aroused considerable interest from scientists recently because of its simple design, low manufacturing cost and environmental friendliness. A general DSSC contains a $TiO_2$ photoanode, a counter electrode (CE) and an electrolyte consisting of a redox medium, such as iodine/triiodide ($I^-/I_3^-$).[3–6] The counter electrode plays an instrumental part in the catalytic reduction process of $I_3^-$. Platinum (Pt) is a traditional CE material owing to its high electrocatalytic properties and favourable electrical behaviour.[7] But, the high price of Pt limits its commercial use as a counter-electrode.[7,8] Therefore, it is of great relevance to explore a counter electrode material with abundant resources and superior performance to replace the precious metal, in order to promote the wide application of DSSCs.[9–11]

To date, many catalytically active materials have attracted the interest of researchers. Transition metal sulfides (TMSs) and their complexes have also attracted attention due to their unique electrical properties and excellent electrochemical reactivity.[12,13] One promising catalytic material is iron sulphide. Iron sulphides are widely distributed and readily available in nature, and $Fe_7S_8$ has attracted the attention of scientists because of its high iron content, which is beneficial for electrochemical catalysis.[13–15] For example, Y. J. Zhang *et al.* reported dual-carbon-confined $Fe_7S_8$ materials as lithium battery anodes with excellent rate performance and stability.[16] However, the poor electrical conductivity of sulfides limits their development in the field of catalysis. Graphene has become an increasingly important material for nanotechnology research owing to its good electrical conductivity and excellent stability in electrochemical environments.[14] For example, J. Yao *et al.* reported the construction of NHCS/NiS/rGO nanocomposites by immobilizing NiS nanosheets on the surface of NHCS and then encapsulating them with rGO, which the PCE of NHCS/NiS/rGO CE in DSSCs is 9.32%.[17] TMSs combined with rGO, carbon nanotubes and other carbonaceous materials can improve the stability and electrochemical activity of TMSs.[14,18] Therefore, the effective coupling of rGO with sulfide would be a promising option to greatly facilitate $I_3^-$ reduction and improve PCE.

---

[a] *School of Materials Science and Engineering, Anhui Key Laboratory of Information Materials and Devices, Institute of Physical Science and Information Technology, Anhui University, Hefei 230601, People's Republic of China. E-mail: liguang1971@ahu.edu.cn*

[b] *School of Physics and Optoelectronic Engineering, Anhui University, Hefei 230601, People's Republic of China. E-mail: jinsw@mail.ustc.edu.cn*

[c] *Anhui Province Key Laboratory of Simulation and Design for Electronic Information System, Universities Joint Key Laboratory of Photoelectric Detection Science and Technology in Anhui Province, Hefei Normal University, Hefei, 230601, People's Republic of China*

† Electronic supplementary information (ESI) available. See DOI: **https://doi.org/10.1039/d3ra02457a**

Herein, $Fe_7S_8$ nanospheres were prepared by hydrothermal method combined with sulfidation; and then compounded with different amounts of rGO to obtain $Fe_7S_8$@rGO-*x* ($x = 10$, 15, 20, 25, 30, 40 wt%; denotes rGO as a percentage by mass of $Fe_7S_8$) composites. Characterization tests show the porous structure of $Fe_7S_8$@rGO. The abundant nanopores enhance the contact area of the $I_3^-$ ions and provide more reactive sites for the reduction of the $I_3^-$ ions. Photocurrent density voltage (*J*–*V*) test indicated that $Fe_7S_8$@rGO-20 wt% CE had the best power conversion efficiency (PCE) among all samples (8.40%). It's higher than the $Fe_7S_8$ (7.60%), $Fe_7S_8$@rGO-10 wt% (7.82%), $Fe_7S_8$@rGO-15 wt% (8.20%), $Fe_7S_8$@rGO-25 wt% (8.25%), $Fe_7S_8$@rGO-30 wt% (7.81%), $Fe_7S_8$@rGO-40 wt% (7.49%) and the conventional Pt CE (7.69%). Test results for all samples are also presented in the ESI.† The presence of rGO enhances the specific surface area and is more favorable for charge transfer. These results suggest that compounding iron-based sulfides with carbon materials is a promising option.

## 2. Experimental section

### 2.1. Materials

Ferric nitrate nonahydrate ($Fe(NO_3)_3 \cdot 9H_2O$), glycerol, isopropyl alcohol, absolute ethanol, polyethylene glycol (PEG 20000), nitric acid ($HNO_3$), sulfuric acid ($H_2SO_4$), potassium permanganate ($KMnO_4$), hydrogen peroxide ($H_2O_2$), sulphur powder and graphite powder were bought from Macklin. Lithium iodide (LiI), lithium perchlorate ($LiClO_4$) and tetrabutyl ammonium iodide, 4-*tert*-butyl pyridine, acetonitrile, were obtained from Aladdin. All the chemical-grade agents were commercially purchased without further purification.

### 2.2. Synthesis of $Fe_7S_8$ microspheres

Typically, 7.5 mL of glycerol was mixed into 52.5 mL of isopropanol and stirred for 30 min using a magnetic stirring station. Glycerol has a high solubility for many compounds and prevents unwanted chemical reactions from occurring in solution. IPA has a high solubility for esters. Subsequently, 0.5 mmol of $Fe(NO_3)_3 \cdot 9H_2O$ was added to the above solution at once, and then magnetic stirring was continued for 1 h to obtain an orange solution. Transfer the mixture to the reaction kettle and hold at 160 °C for 10 h. In addition, 140 °C and 180 °C were tested, but the results were not satisfactory. After the reaction was complete, the reaction kettle was cooled to room temperature overnight, the samples were washed 5 to 6 times alternately with anhydrous ethanol and deionized water, and the yellow-green precipitate was obtained after centrifugation at 4000 rpm and dried under vacuum in an oven at 60 °C for 12 h to obtain the Fe-glycerate precursors. After that, 20 mg of sulfur powder was weighed in a quartz boat and placed near the inlet end of the tube furnace, and then a quartz boat containing 100 mg of iron glycerate precursor was placed at the outlet end, and the sample was continuously burned in nitrogen at 500 °C for 2 h at a temperature gradient of 3 °C $min^{-1}$. Finally, we obtained $Fe_7S_8$ nanomaterials.

### 2.3. Preparation of $Fe_7S_8$@rGO-*x* nanocomposite

The $Fe_7S_8$@rGO-*x* nanocomposites were obtained by a facile hydrothermal route. A flow chart for the production of $Fe_7S_8$@rGO-*x* is shown in Fig. 1a. First, GO (10 mg, the weight percentage is 20 wt%) were taken in four 100 mL beakers, all of which were added with 30 mL of anhydrous ethanol and sonicated for 4 hours. Subsequently, 50 mg of $Fe_7S_8$ was added to the above four solutions, stirred continuously overnight, and then transferred to a Teflon autoclave and held at 160 °C for 8 h. Cool naturally to room temperature after the reaction, washed and centrifuged, and dried in an oven at 60 °C for 12 h to obtain $Fe_7S_8$@rGO-20 wt%. Other different components are represented in the ESI.†

### 2.4. The manufacture of DSSCs

In general, the DSSC is made up of a dye-sensitized photoanode $TiO_2$, a counter electrode with a liquid electrolyte. First, the commercially available $TiO_2$ was placed in N719 dye and sensitized at room temperature at the dark level for 20 h. The sensitized $TiO_2$ was removed, rinsed with ethanol, allowed to dry naturally, and then the transparent adhesive tape was applied to both ends of the $TiO_2$. The photoanode $TiO_2$ and CE were held together, and injected electrolytes to fill the void between them. The electrolyte consists of 0.6 mol 1-propy1-2,3-dimethylimidazolium iodide, 0.5 M LiI, 0.05 mol $I_2$, and 0.5 M 4-*tert*-butyl pyridine. The CEs include $Fe_7S_8$, $Fe_7S_8$@rGO-*x* and commercially available Pt. It has to be noted that all equipment other than CEs was obtained from the commercial market. The preparation of the electrodes and the instrumentation for the characterization are shown in the ESI.†

## 3. Result and discussion

### 3.1. Morphology and structure

The microstructure of samples can be clearly observed by scanning electron microscopy (SEM) and transmission electron microscopy (TEM). The SEM image of homogeneous solid Fe-glycerate nanospheres is shown in Fig. 1b. The surface of the prepared Fe-glycerate microspheres contains a large number of nanosheets, which are uniformly distributed with about 500 nm in size. Fig. 1c shows that the Fe-glycerate precursor is a solid sphere with tiny nanosheets interspersed on its surface. The $Fe_7S_8$ obtained after sulphation is illustrated in Fig. 1d, and it's also noted that the nanospheres after vulcanization and sintering still maintain their basic morphology without deformation, indicating that the samples exhibit good morphological stability. Meanwhile, it can also be found that the number of nanosheets on the surface of $Fe_7S_8$ is more abundant, which allows it to provide a larger specific surface area, which can enable an increased exposure of the active site. It is noteworthy that $Fe_7S_8$ spherical nanoflowers are encapsulated inside graphene and are shown in Fig. 1e, where the $Fe_7S_8$ and rGO are coupled to each other to form fast channels for electron transfer, in addition to the fact that this encapsulated structure makes $Fe_7S_8$ less susceptible to corrosion. As can be seen by TEM in Fig. 1f, the surface of the nanospheres was rougher. In addition, Fig. 1g

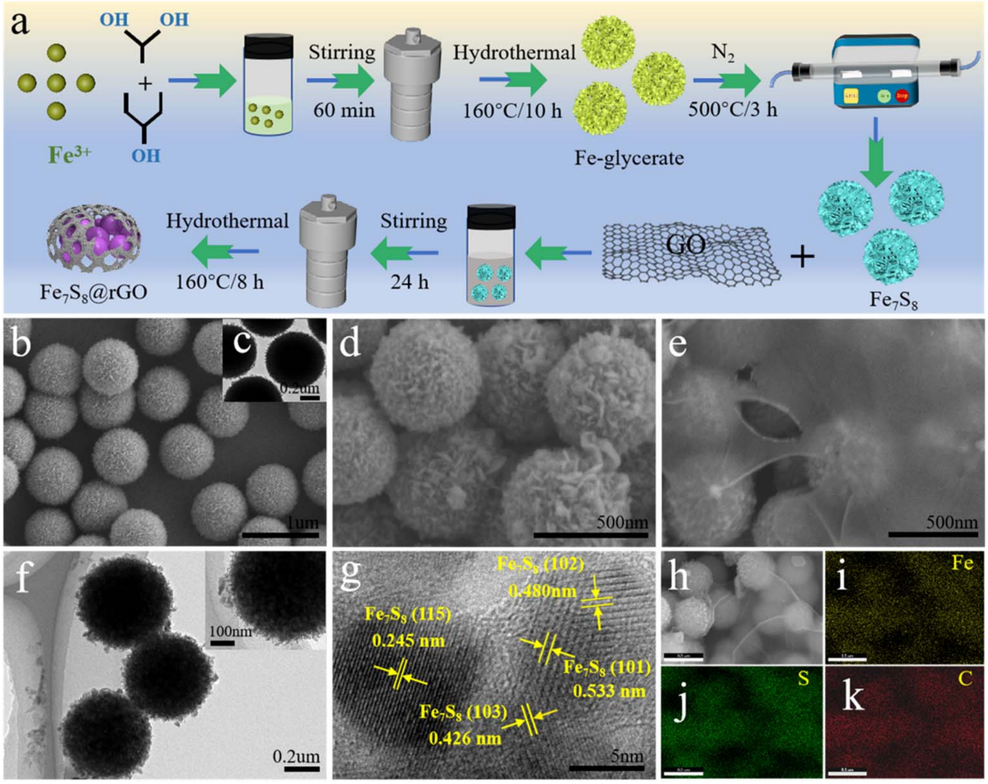

Fig. 1 (a) Synthesis process of $Fe_7S_8$@rGO-*x*. (b) SEM image of Fe-glycerate precursors. (c) The TEM image of Fe-glycerate precursors. SEM images of (d) $Fe_7S_8$, (e) $Fe_7S_8$@rGO-20 wt%. (f) TEM image, (g) HRTEM image of $Fe_7S_8$@rGO-20 wt%. (h–k) SEM images of $Fe_7S_8$@rGO-20 wt% and corresponding EDX element distribution.

presents the high-resolution TEM (HRTEM) image of the $Fe_7S_8$@rGO-20 wt% composite. Fig. 1g clearly shows multiple lattice fringes with spacings of 0.245 nm, 0.426 nm, 0.480 nm, and 0.533 nm corresponding to the (115), (103), (102), and (101) crystal planes of $Fe_7S_8$, respectively, which indicates the good crystallinity of the as-prepared sample. To further identify the existence of Fe, S and C elements in $Fe_7S_8$@rGO-20 wt% composites, the distribution of each component was analyzed by elemental mapping. As depicted in Fig. 1h–k, the presence and uniform distribution of Fe, S and C can be found in the energy dispersive X-ray (EDX) mapping.

The crystal structure and composition of the prepared materials were determined by X-ray diffraction (XRD) analysis. As exhibited in Fig. 2a, from the XRD pattern of $Fe_7S_8$@rGO-20 wt%, a broad diffraction peak near 23.8° can be noted. This diffraction peak corresponds to the (002) crystal plane of carbon, which indicates the highly crystalline structure of rGO.[19] Meanwhile, typical diffraction peaks at around 30.0°, 33.9°, 53.4°, 57.6°, 64.8°, and 71.6°, which correspond to the (200), (203), (305), (209), (403) and (406) crystal planes of $Fe_7S_8$ (JCPDF, 24-0220), respectively.[20,21] The main diffraction peak of the $Fe_7S_8$@rGO-20 wt% composite is the same as pure $Fe_7S_8$, with a slight weakening of the peak intensity due to the introduction of graphene.

To further confirm the presence of graphene oxide in $Fe_7S_8$@rGO-20 wt% composites, it was characterized by Raman spectroscopy with an excitation wavelength of 532 nm. The Raman spectra of rGO and $Fe_7S_8$@rGO-20 wt% are displayed in Fig. 2b. In the Raman spectrum, there are two Raman peaks at 1348 $cm^{-1}$ (D band) and 1580 $cm^{-1}$ (G band) due to the disordered carbon atoms and the $sp^{2-}$ bonded carbon.[22,23] The ratio $I_D : I_G$ is commonly applied to measure internal defects in a material, with higher ratios indicating a greater number of defective sites inside the material.[10,17,24] It can be observed in the figure that the $I_D/I_G$ of $Fe_7S_8$@rGO-20 wt% is 1.04, while the $I_D/I_G$ of rGO is 0.93, indicating that the $Fe_7S_8$@rGO-20 wt% composite has more defects, which would be more conducive to the catalytic reaction.

Additionally, the specific surface area and pore size of $Fe_7S_8$@rGO-20 wt% were examined by $N_2$ adsorption–desorption isotherm. The test results are displayed in Fig. 2c and d. The specific surface area of $Fe_7S_8$@rGO-20 wt% can be obtained as 64.9 $m^2$ $g^{-1}$ based on the calculation of Brunauer–Emmett–Teller (BET). Using the Barrett–Joyner–Halenda (BJH) method to analyze the pore size, the average pore size of $Fe_7S_8$@rGO-20 wt% composites is about 12.7 nm. The larger surface area can expand the contact surface with the electrolyte to increase the number of active sites, and the larger pore size will shorten the diffusion path of ions. The porous structure of $Fe_7S_8$@rGO-20 wt% ensures better penetration of the electrolyte and further promotes the diffusion of redox pairs, expanding the possibility of efficient transport between electrons and ions, which is beneficial for improving the electrochemical performance of the material.

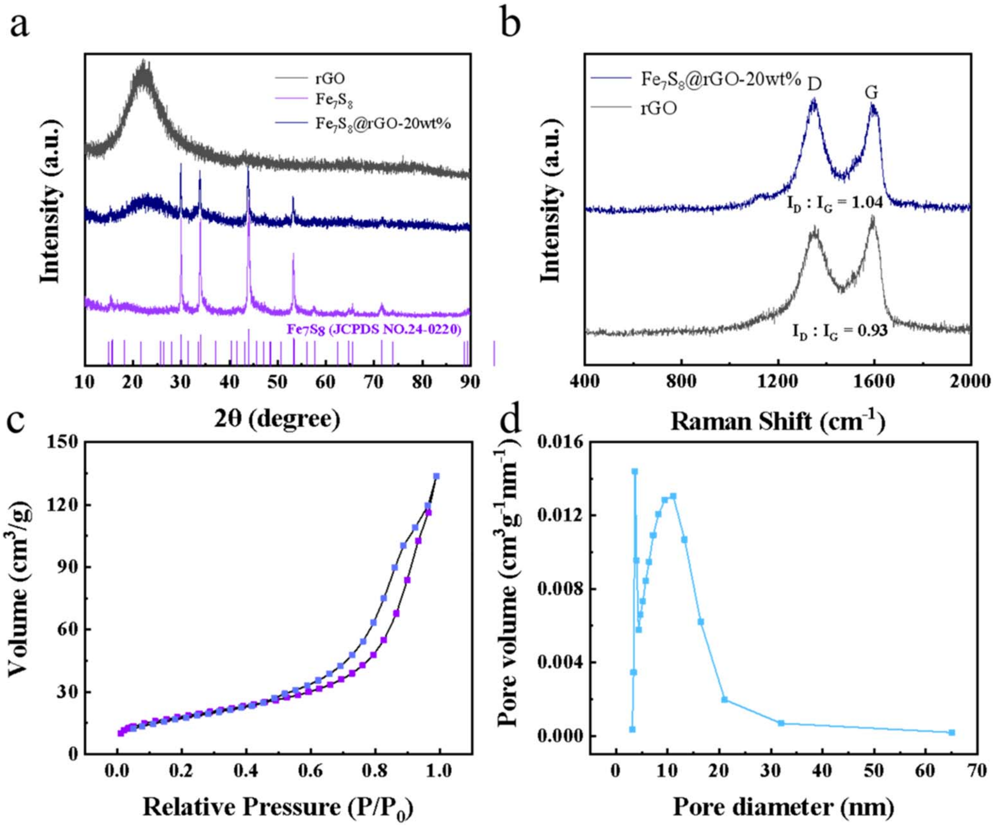

Fig. 2 (a) XRD patterns of rGO, $Fe_7S_8$, and $Fe_7S_8$@rGO-20 wt%. (b) Raman spectra of rGO and $Fe_7S_8$@rGO-20 wt%. (c) $N_2$ adsorption–desorption isotherm of $Fe_7S_8$@rGO-20 wt%. (d) The pore size distribution of $Fe_7S_8$@rGO-20 wt%.

The chemical state of the characteristic elements on the $Fe_7S_8$@rGO-20 wt% surface was surveyed by X-ray photoelectron spectroscopy (XPS). Fig. 3a shows the total spectrum of $Fe_7S_8$@rGO-20 wt%, from which it can be noted that the complex is composed of Fe, S, C and O. The spectra of Fe 2p, S 2p and C 1s in $Fe_7S_8$@rGO-20 wt% are shown in Fig. 3b–d, respectively. In the spectrum of Fe 2p, the presence of three chemical states of Fe can be clearly revealed. The binding energies at 711.1 eV and 724.7 eV are attributed to the presence of $Fe^{2+}$ species, while the binding energies at 712.9 eV and 726.7 eV are due to the presence of $Fe^{3+}$ in the material.[22–26] The binding energy at 707.6 eV corresponds to the metal $Fe^0$, which may be formed due to the reduction of iron ions by carbon during hydrothermal processes. In addition, two oscillating satellite peaks at 719.8 eV and 732.8 eV can be expected. The S 2p spectrum is given in Fig. 3c. The peaks at 161.7 eV, 163.9 eV and 165.0 eV correspond to $S^{2-}$, while the broad peak at 168.8 eV is attributed to $SO_x^{2-}$, which is caused by the oxidation of $S^{2-}$ when the specimen is exposed to air.[23] For the C 1s spectrum of $Fe_7S_8$@rGO-20 wt% composite, the binding energy locate at 284.8 eV, 286.1 eV and 289.2 eV correspond to carbon shell C–C, C–O, C=O, respectively.[23,26]

## 3.2. Electrochemical and photovoltaic characterizations

To investigate the transport kinetics of the material, Tafel polarization measurements were made using self-assembled symmetric cells with two identical electrodes (CE/electrolyte/CE).[27] Tafel polarization consists of two basic indicators: the exchange current density ($J_0$) and the limiting diffusion current density ($J_{\lim}$). $\log J_0$ can be acquired through the crossover point of the cathode branch and zero voltage. And the intersection of the cathode branch and the vertical pole in the Tafel curve can be seen as $\log J_{\lim}$. $J_0$ is an accurate indicator of electrochemical reactivity and a large $J_0$ corresponds to a high catalytic performance of CE for the reduction of $I_3^-$. $J_{\lim}$ is positively correlated with the diffusion coefficient $D$. The Tafel curves for the different CEs are presented in Fig. 4a. $J_0$ and $J_{\lim}$ for each sample are obtained from the curves as shown in Table 1. It is worth remarking that CE configured with $Fe_7S_8$@rGO-20 wt% reached higher $\log J_0$ (0.64 mA cm$^{-2}$) and $\log J_{\lim}$ (1.68 mA cm$^{-2}$), much higher than Pt (0.38 mA cm$^{-2}$, 1.49 mA cm$^{-2}$). The results indicated that $Fe_7S_8$@rGO-20 wt% has better catalytic activity for the reduction of $I_3^-$.

Electrochemical impedance spectrum (EIS) is also another measure for catalytic activity at counter electrodes, which like the Tafel polarization needs to be tested with a simulated symmetric cell. As shown in Fig. 4b, a typical impedance spectrum generally consists of two approximate semicircles. The intercept on the horizontal axis in the high-frequency region represents the series resistance ($R_s$), which is related to the electrical conductivity of the material. The first semicircle in the high-frequency region represents the impedance ($R_{ct}$) of the

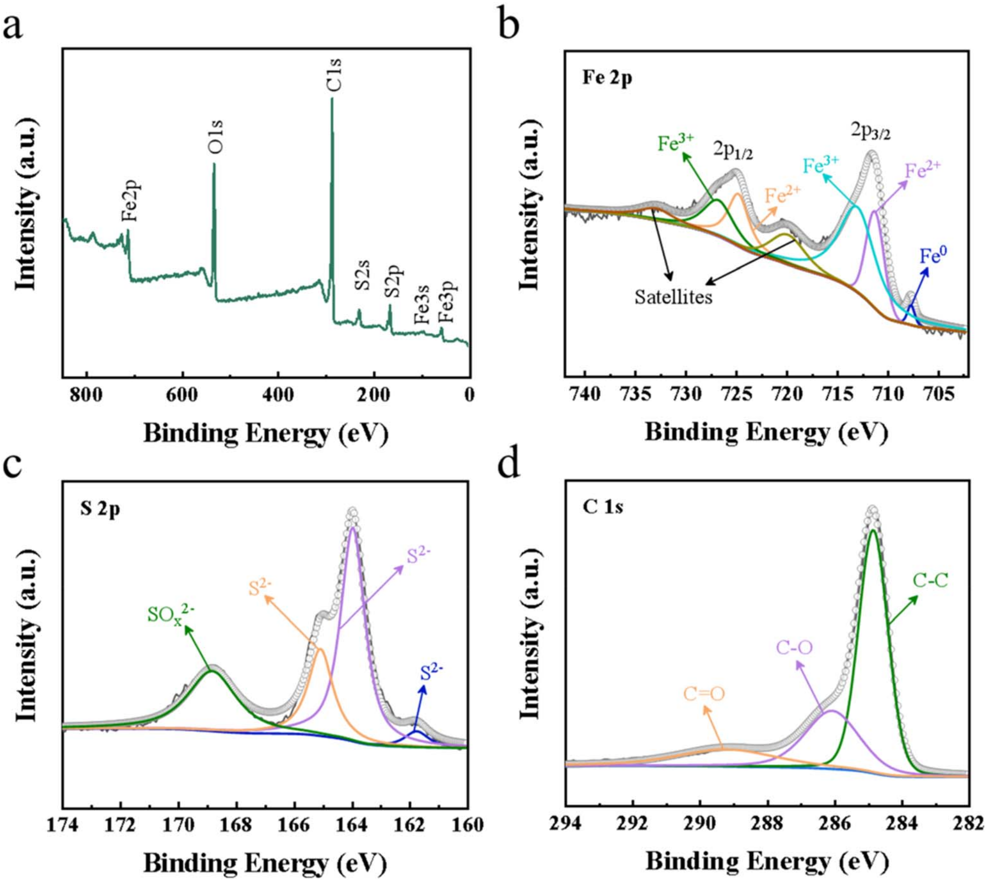

Fig. 3 (a) Wide XPS spectra of $Fe_7S_8$@rGO-20 wt%. (b) Fe 2p, (c) S 2p, and (d) C 1s spectra.

charge transfer between the electrode and electrolyte interface and the other semicircle represents the diffusion impedance ($Z_N$). The corresponding $R_s$ and $R_{ct}$ for each sample are summarized in Table 1. The smallest $R_s$ for $Fe_7S_8$@rGO-20 wt% is about 6.38 Ω $cm^2$, which is lower than Pt (9.59 Ω $cm^2$), rGO (7.64 Ω $cm^2$), $Fe_7S_8$ (6.84 Ω $cm^2$). The sequence of the $R_{ct}$ values is $Fe_7S_8$@rGO-20 wt% < Pt < rGO < $Fe_7S_8$ CEs, which means that the introduction of rGO can improve the conductivity. Through comparison, it is found that $Fe_7S_8$@rGO-20 wt% possesses the smallest transfer impedance, proving that it has the best catalytic activity. This is because the porous structure of $Fe_7S_8$ enhances the penetration of electrolyte ions, thus facilitating the diffusion of $I_3^-$, and the synergistic effect between graphene and $Fe_7S_8$ promotes the rapid transfer of electrons.

To investigate the photovoltaic performance of each material, comparative tests were conducted and the *J*–*V* curves for samples are shown in Fig. 4d. The specific data on photovoltaic (PV) parameters such as open-circuit voltage ($V_{oc}$), fill factor (FF), short-circuit current density ($J_{sc}$) acquired from the tests are clearly shown in Table 2, and after obtaining these parameters the corresponding PCE can be calculated by the following eqn (1):

$$\mathrm{PCE} = \frac{\mathrm{FF} J_{sc} V_{oc}}{P_{in}} \times 100\% \quad (1)$$

The difference of PCE mainly comes from the photocurrent density ($J_{sc}$), and the change of $J_{sc}$ is mainly due to the difference of the catalytic ability of the electrode, so the electrocatalytic reduction of $I_3^-$ on the CE surface is a rate-determining step in DSSCs.[28–31] Impressively, the $Fe_7S_8$@rGO-20 wt%-based CE reached PCE (8.40%), which is higher than $Fe_7S_8$ (7.60%), rGO (4.28%), and Pt (7.69%). The PCE of $Fe_7S_8$ CE was significantly smaller than that of Pt CE, but the PCE of the sample was effectively improved after being combined with rGO. It indicates that the PCE of $Fe_7S_8$@rGO-*x* is influenced by the rGO.

The catalytic ability of various CEs to reduce $I_3^-$ was further investigated using cyclic voltammetry tests and the CV curves as shown in Fig. 4d were obtained. Two pairs of oxidation–reduction peaks are visible in the graph for each individual curve, the horizontal axis spacing of the first pair of oxidation–reduction peaks (marked as Ox1 and Red1) being $E_{pp}$.[32,33] A smaller $E_{pp}$ value means that the oxidation and reduction reactions of CV alternate more quickly and smoothly, which in turn improves the catalytic properties of the material for the reduction of $I_3^-$.[32] The coupled peaks Ox1 and Red1 could be described by eqn (2) and (3):

$$3I^- - 2e^- \rightarrow I_3^- \quad (2)$$

$$I_3^- + 2e^- \rightarrow 3I^- \quad (3)$$

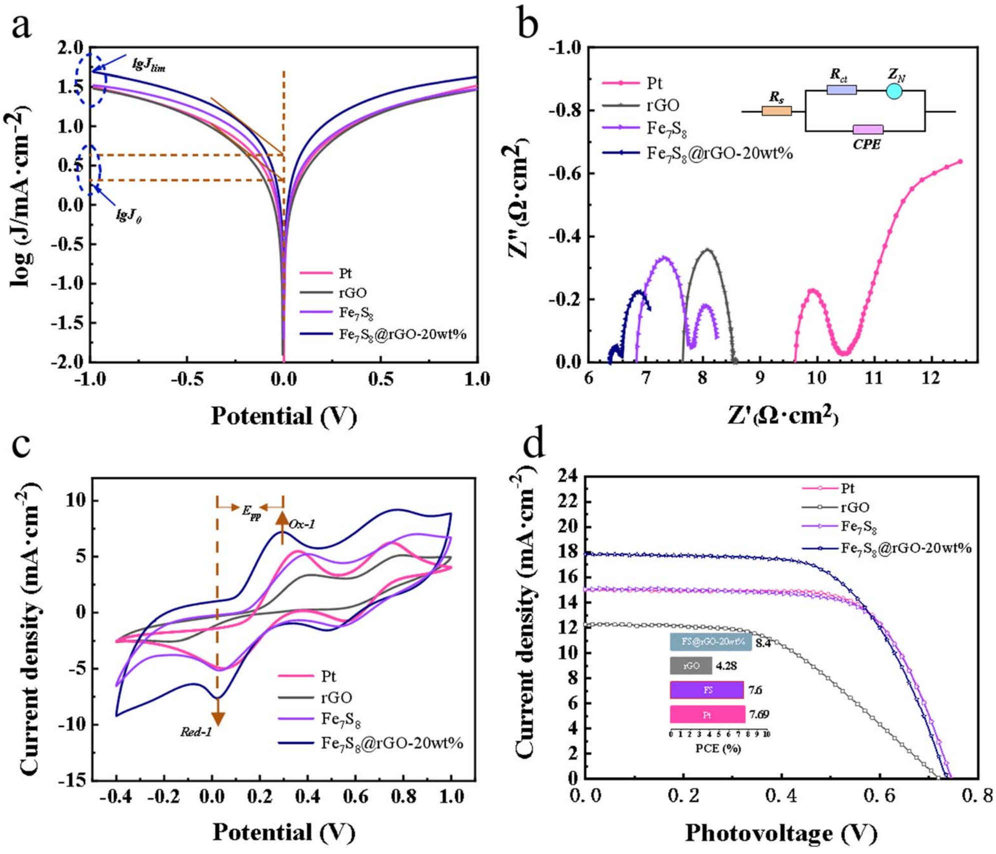

Fig. 4 (a) Tafel polarization curves, (b) Nyquist plots, (c) CV curves, (d) $J$–$V$ curves of Pt, rGO, $Fe_7S_8$, and $Fe_7S_8$@rGO-20 wt% CEs.

Table 1 Electrochemical parameters for different CEs

| CEs | $R_s$ ($\Omega$ cm$^2$) | $R_{ct}$ ($\Omega$ cm$^2$) | $\log J_0$ (mA cm$^{-2}$) | $\log J_{lim}$ (mA cm$^{-2}$) |
|---|---|---|---|---|
| rGO | 7.64 | 0.44 | 0.30 | 1.47 |
| $Fe_7S_8$ | 6.84 | 0.48 | 0.48 | 1.52 |
| $Fe_7S_8$@rGO-20 wt% | 6.38 | 0.08 | 0.64 | 1.68 |
| Pt | 9.59 | 0.43 | 0.38 | 1.49 |

The specific values are listed in Table 2. The graph clearly shows that the $E_{pp}$ of $Fe_7S_8$@rGO CE is significantly smaller than that of Pt CE. $Fe_7S_8$@rGO-20 wt% has the smallest $E_{pp}$ of about 0.27 V, which is higher than Pt (0.33 V), rGO (0.59 V) and $Fe_7S_8$ (0.36 V). In summary, the lowest $E_{pp}$ implies that $Fe_7S_8$@rGO-20 wt% has excellent catalytic reduction activity for $I_3^-$ and can be used as a superior performing CE among DSSCs.

To research the correlation between peak current density and sweep speed in the CV curves, plots of $Fe_7S_8$@rGO-20 wt% were measured at different scan rates. From Fig. 5a, it can be concluded that as the electrochemical polarization increases with increasing sweep speed, the overpotential increases and the reversibility decreases. As illustrated in Fig. 5b, the peak current density is related to the square root of the sweep rate, suggesting that $Fe_7S_8$@rGO-20 wt% is only reacting with the redox medium, while electron diffusion at the interface between the two is limited.[34] Furthermore, stability is also a key parameter to be considered when judging electrode materials.

Table 2 Photovoltaic performance parameters of rGO, $Fe_7S_8$, $Fe_7S_8$@rGO-20 wt%, and Pt CEs

| CEs | $E_{pp}$ (V) | $J_{sc}$ (mA cm$^{-2}$) | $V_{oc}$ (V) | FF (%) | PCE (%) |
|---|---|---|---|---|---|
| rGO | $0.59 \pm 0.01$ | 12.25 | 0.725 | 48.13 | 4.28 |
| $Fe_7S_8$ | $0.36 \pm 0.01$ | 15.05 | 0.745 | 67.75 | 7.60 |
| $Fe_7S_8$@rGO-20 wt% | $0.27 \pm 0.01$ | 17.83 | 0.740 | 63.64 | 8.40 |
| Pt | $0.33 \pm 0.01$ | 15.01 | 0.745 | 68.82 | 7.69 |

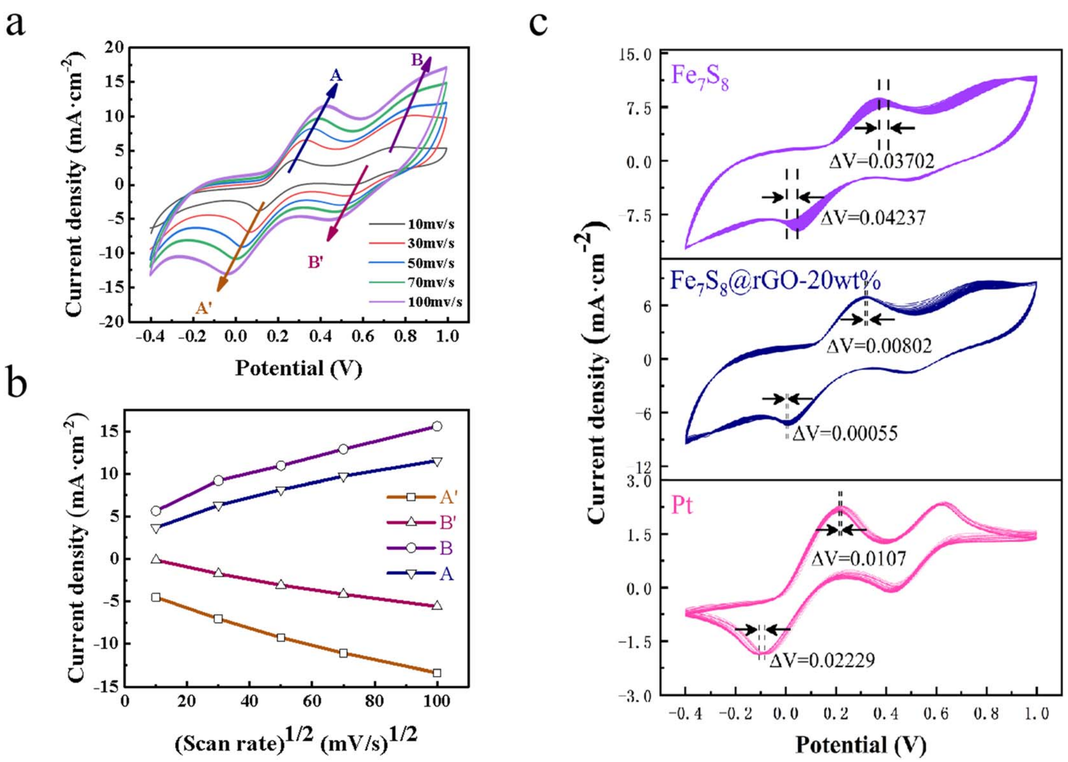

Fig. 5 (a) CV curves of $Fe_7S_8$@rGO-20 wt% CE at different scan rates, (b) peak current densities curve, (c) continuous CV test curves of different CE.

To assess the stability of the samples in the electrolyte, the CV tests were conducted on $Fe_7S_8$, $Fe_7S_8$@rGO-20 wt% and Pt for 25 consecutive cycles at a scan rate of 25 mV s$^{-1}$. As can be seen in Fig. 5c, the current density of $Fe_7S_8$@rGO-20 wt% did not decrease significantly during cycling, the peak spacing shifts were much smaller than those of Pt and $Fe_7S_8$, and the first pair of redox peaks of $Fe_7S_8$@rGO-20 wt% had the best overlap. The presence of rGO reduces the corrosive effect of the electrolyte and helps to improve the electrochemical stability of the material. Thus $Fe_7S_8$@rGO-20 wt% maintains good electrochemical stability as CE for DSSCs. $Fe_7S_8$@rGO-20 wt% may be a promising electrode material in DSSCs.

## 4. Conclusions

In summary, we have successfully synthesized porous $Fe_7S_8$@rGO-*x* composites, and investigated their photovoltaic and electrochemical properties. The experimental results show that $Fe_7S_8$@rGO nanomaterials as CEs perform better than Pt in DSSCs. The PCE of the DSSCs assembled by $Fe_7S_8$@rGO-20 wt% can reach 8.40%, which is better than that of Pt (7.69%). The excellent performance is on the one hand due to the abundant nanopores and large specific surface area, which enhances the contact area with $I_3^-$ and provides more active sites for charge transfer and reduction of $I_3^-$. On the other hand, the hybridization of $Fe_7S_8$ with rGO facilitates charge transfer and reaction kinetics. And cycle stability tests indicate that the electrochemical stability of the $Fe_7S_8$@rGO-20 wt% composite is also superior to that of Pt. This is because the presence of rGO reduces the corrosion of the sample by the electrolyte. Such excellent properties indicate that $Fe_7S_8$@rGO composite may be a very promising CE material. The research also offers a hopeful idea for effectively improving the performance of DSSCs.

## Conflicts of interest

There are no conflicts to declare.

## Acknowledgements

This work was financially supported by the National Key R&D Program of China (2017YFA0403503), the National Natural Science Foundation of China (11674001), the Key Projects of Natural Science Research in Universities of Anhui Province (KJ2020A0018), the Key Natural Science Research Program of Anhui Educational Committee (KJ2018ZD001), 2021 Post-graduate Research Project in Universities – Transition Metal Compounds in Dye Sensitized Solar Cells, Bi-Directional Application of Oxygen Precipitation Reaction (Y020410004).

## References

1 C. Zhao, N. Li, R. Zhang, Z. Zhu, J. Lin, K. Zhang and C. Zhao, *ACS Appl. Mater. Interfaces*, 2019, **11**, 47858–47867.
2 H. Fu, Z. Li, Z. Liu and Z. Wang, *Sustainability*, 2018, **10**, 2488.
3 C. Zhang, L. Deng, P. Zhang, X. Ren, Y. Li and T. He, *Electrochim. Acta*, 2017, **229**, 229–238.

4 B. Kilic, S. Turkdogan, O. C. Ozer, M. Asgin, O. Bayrakli, G. Surucu, A. Astam and D. Ekinci, *Mater. Lett.*, 2016, **185**, 584–587.

5 J. Qiu, D. He, R. Zhao, B. Sun, H. Ji, N. Zhang, Y. Li, X. Lu and C. Wang, *J. Colloid Interface Sci.*, 2018, **522**, 95–103.

6 W. Zhang, R. Zhu, L. Ke, X. Liu, B. Liu and S. Ramakrishna, *Small*, 2010, **6**, 2176–2182.

7 Q. Wang, Y. Wang, P. Wei, X. Liu and L. Duan, *Appl. Surf. Sci.*, 2019, **494**, 1–7.

8 A. Sarkar, S. Bera and A. K. Chakraborty, *Sol. Energy*, 2020, **208**, 139–149.

9 S. Lu, M. Chen, Y. Wang, R. Li, J. Lin and X. Zhang, *Sol. Energy*, 2021, **220**, 788–795.

10 Q. Yang, X. Zuo, J. Yao, K. Zhang, H. Zhang, M. W. Khan, W. Wang, H. Tang, M. Wu, G. Li and S. Jin, *J. Electroanal. Chem.*, 2019, **844**, 34–42.

11 K. Xiong, G. Li, C. Jin and S. Jin, *Mater. Lett.*, 2016, **164**, 609–612.

12 J. Ma, W. Shen and F. Yu, *J. Power Sources*, 2017, **351**, 58–66.

13 A. Sarkar, A. K. Chakraborty and S. Bera, *Sol. Energy Mater. Sol. Cells*, 2018, **182**, 314–320.

14 R. Kang, S. Li, B. Zou, X. Liu, Y. Zhao, J. Qiu, G. Li, F. Qiao and J. Lian, *J. Alloys Compd.*, 2021, **865**, 158824.

15 N. Cheng, X. Chen, L. Zhang and Z. Liu, *J. Energy Chem.*, 2021, **54**, 604–611.

16 Y. J. Zhang, W. Chang, J. Qu, S. M. Hao, Q. Y. Ji, Z. G. Jiang and Z. Z. Yu, *Chemistry*, 2018, **24**, 17339–17344.

17 J. Yao, W. Wang, X. Zuo, Q. Yang, M. W. Khan, M. Wu, H. Tang, S. Jin and G. Li, *Appl. Catal., B*, 2019, **256**, 117857.

18 Z. Zhao, X. Teng, Q. Xiong, H. Chi, Y. Yuan, H. Qin and Z. Ji, *Sustainable Mater. Technol.*, 2021, **29**, e00313.

19 B. Liu, F. Zhang, Q. Wu, J. Wang, W. Li, L. Dong and Y. Yin, *Mater. Chem. Phys.*, 2015, **151**, 60–65.

20 M. J. Choi, J. Kim, J. K. Yoo, S. Yim, J. Jeon and Y. S. Jung, *Small*, 2018, **14**, 1–6.

21 Y. Wang, Z. Wen, C. C. Wang, C. C. Yang and Q. Jiang, *Small*, 2021, **17**, 1–10.

22 L. Shi, D. Li, J. Yu, H. Liu, Y. Zhao, H. Xin, Y. Lin, C. Lin, C. Li and C. Zhu, *J. Mater. Chem. A*, 2018, **6**, 7967–7976.

23 F. Jiang, Q. Wang, R. Du, X. Yan and Y. Zhou, *Chem. Phys. Lett.*, 2018, **706**, 273–279.

24 F. Du, X. Zuo, Q. Yang, G. Li, Z. Ding, M. Wu, Y. Ma and K. Zhu, *J. Mater. Chem. C*, 2016, **4**, 10323–10328.

25 Y. He, Y. Xu, J. Li, Z. Xu, Z. Zhang, J. Sun, M. Zhang, X. Zhu and X. Zhou, *Energy Fuels*, 2021, **35**, 3490–3496.

26 Q. Zhang, J. Liao, M. Liao, J. Dai, H. Ge, T. Duan and W. Yao, *Appl. Surf. Sci.*, 2019, **473**, 799–806.

27 J. Yao, K. Zhang, W. Wang, X. Zuo, Q. Yang, H. Tang, M. Wu and G. Li, *ACS Appl. Mater. Interfaces*, 2018, **10**, 19564–19572.

28 I. T. Chiu, C. T. Li, C. P. Lee, P. Y. Chen, Y. H. Tseng, R. Vittal and K. C. Ho, *Nano Energy*, 2016, **22**, 594–606.

29 M. Gurulakshmi, A. Meenakshamma, K. Susmitha, N. Charanadhar, V. V. S. S. Srikanth, S. Narendra Babu, Y. P. Venkata Subbaiah, K. Venkateswarlu and M. Raghavender, *Sol. Energy*, 2019, **193**, 568–575.

30 S. Yun, A. Hagfeldt and T. Ma, *Adv. Mater.*, 2014, **26**, 6210–6237.

31 A. Listorti, B. O'Regan and J. R. Durrant, *Chem. Mater.*, 2011, **23**, 3381–3399.

32 L. Shao, X. Qian, H. Li, C. Xu and L. Hou, *Chem. Eng. J.*, 2017, **315**, 562–572.

33 W. Wang, X. Zuo, Q. Yang, Q. Yang, H. Tang, H. Zhang and G. Li, *Appl. Catal., B*, 2022, **300**, 120726.

34 W. Hou, Y. Xiao, G. Han and H. Zhou, *Electrochim. Acta*, 2016, **190**, 720–728.